



OPEN

Unraveling the impact of microwave-assisted techniques in the fabrication of yttrium-doped TiO₂ photocatalyst

Adam Kubiak & Michał Cegłowski

In this study, we investigate the role of microwave technology in the fabrication of yttrium-doped TiO₂ through a comparative analysis of hydrothermal techniques. Microwave-assisted hydrothermal synthesis offers advantages, but a comprehensive comparison between microwave-assisted and conventional methods is lacking. Therefore, in our investigation, we systematically evaluate and compare the morphological, structural, and optical properties of yttrium-doped TiO₂ samples synthesized using both techniques. The X-ray diffraction (XRD) patterns confirm the anatase tetragonal structure of the synthesized TiO₂-Y systems, while the larger ion radius of yttrium (Y³⁺) compared to titanium (Ti⁴⁺) presents challenges for yttrium to incorporate into the TiO₂ lattice. The X-ray Photoelectron Spectroscopy (XPS) revealed a significant difference in the atomic content of yttrium between the TiO₂-Y systems synthesized using microwave-assisted and conventional methods. This finding suggests that the rapid microwave method is more effective in successfully doping TiO₂ with rare earth metals such as yttrium. The photo-oxidation of carbamazepine (CBZ) using TiO₂-Y systems demonstrated high efficiency under UV-LED light. Microwave-synthesized TiO₂-Y demonstrates improved photo-oxidation efficiency of CBZ, attributed to enhanced absorption, charge transfer, surface area, and crystallite size. Overall, the microwave-synthesized TiO₂-Y systems showed promising performance for the photo-oxidation of CBZ, with improved efficiency compared to conventional synthesis methods.

Titanium dioxide has garnered significant attention in research due to its remarkable photocatalytic properties, chemical stability, and wide availability¹. However, it also has inherent limitations that impede its full potential. One such drawback is its wide band gap, which restricts its photocatalytic activity to the ultraviolet (UV) region^{2,3}. Additionally, TiO₂ exhibits a high recombination rate of photogenerated electron-hole pairs, diminishing its overall photocatalytic efficiency. These limitations hinder the effective utilization of photogenerated charge carriers for desired photocatalytic reactions⁴. To overcome these challenges, researchers have turned to dope TiO₂ nanostructures with rare earth metals. Rare earth metals offer the potential to enhance the surface, optical, and photocatalytic properties of TiO₂. They possess vacant 4f orbitals that readily interact with functional groups, and their incorporation introduces more oxygen defects, effectively suppressing electron-hole recombination during transfer^{5,6}. Moreover, rare earth doping increases impurity levels, leading to more efficient utilization of photo-induced carriers. Doping with rare earth ions, particularly those with 4f electron configurations, significantly enhances adsorption capacity and the rate of photogenerated carrier separation^{7,8}. Among the rare earth elements, yttrium (Y) is a representative candidate. The crystal structure of TiO₂ favors the replacement of Ti⁴⁺ ions with Y³⁺ ions over substituting O₂⁻ with any other anion^{9,10}. This preference arises from differences in charge states and ionic radii. Yttrium possesses unique electronic and chemical characteristics that can influence the structural, optical, and photocatalytic properties of TiO₂^{11,12}. Researchers have explored different synthesis methods to achieve precise control over the doping process, including conventional hydrothermal techniques and microwave-assisted hydrothermal synthesis.

Hydrothermal synthesis is a method that utilizes high temperatures and pressures in an aqueous environment to facilitate the formation of desired materials^{13,14}. Khan et al.¹⁵, emphasized the benefits of this method by illustrating its ability to synthesize Sm³⁺ doped rutile TiO₂ nanorods decorated with GdFeO₃ nanorods for efficient CO₂ conversion and organic pollutants degradation. Additionally, this technique is versatile, as seen in

Faculty of Chemistry, Adam Mickiewicz University, Poznan, Uniwersytetu Poznanskiego 8, 61614 Poznan, Poland.
 email: adam.kubiak@amu.edu.pl

its production of mediator-free hollow BiFeO₃ spheres and porous g-C₃N₄ photocatalysts for both CO₂ conversion and Alizarin Red S degradation. These examples undoubtedly highlight its significant potential¹⁶. However, one challenge in hydrothermal synthesis is maintaining uniform temperature distribution throughout the reaction mixture¹⁷. Temperature gradients can occur within the reactor, potentially leading to variations in material properties or incomplete reactions. To address this issue, microwave-assisted hydrothermal synthesis has emerged as a promising approach, particularly in the fabrication of TiO₂-based materials^{18–20}. Microwave technology provides rapid and efficient heating, resulting in accelerated reaction kinetics and reduced synthesis times compared to conventional heating methods. The selective heating achieved through microwave irradiation can improve homogeneity and enhance material properties^{21,22}. Nevertheless, it is important to consider the potential drawbacks associated with microwave-assisted hydrothermal synthesis. The rapid and intense heating provided by microwaves can sometimes induce unintended side reactions or undesired product selectivity^{23,24}. Localized overheating or thermal gradients caused by microwave radiation may affect reaction pathways and product distribution. Moreover, it should be noted that microwave synthesis relies on the selective heating of materials by microwave radiation²⁵. Achieving efficient heat transfer throughout the sample can be challenging, especially for larger volumes or materials with low microwave absorption²⁶. Non-uniform heating can lead to uneven reactions and incomplete product formation. Therefore, careful optimization of microwave parameters and reaction conditions is necessary to mitigate these challenges and maximize the benefits of microwave-assisted hydrothermal synthesis. Understanding the trade-offs and potential limitations is essential in effectively utilizing this technique to synthesize yttrium-doped TiO₂ and other materials^{27–29}.

This publication presents a novel study that investigates the role of microwave technology in the fabrication of yttrium-doped TiO₂. It does so by conducting a head-to-head comparison with conventional hydrothermal techniques. Through a comprehensive analysis, the study examines the impact of microwave-assisted hydrothermal synthesis on the structural characteristics, optical properties, and photocatalytic performance of yttrium-doped TiO₂ materials. By comparing the outcomes with those obtained through conventional hydrothermal methods, the research offers valuable insights into the impact of microwave technology on the synthesis process and resulting material properties. The findings contribute to our understanding of how microwave technology can enhance the fabrication of yttrium-doped TiO₂ materials. This study represents an important advancement in the field of TiO₂ photocatalysis, highlighting the scientific and technological progress achieved through the integration of microwave technology in the fabrication of yttrium-doped TiO₂.

Materials and methods

Materials

Titanium(IV) chloride (97%), urea (p.a.), yttrium(III) chloride hexahydrate (99%), ammonium oxalate (99%), silver nitrate (>99%), tert-butyl alcohol (99%) benzoquinone (p.a.), and carbamazepine (analytical standard) were purchased from Merck. All reagents were of analytical grade and used without any further purification. The water used in all experiments was deionized.

Synthesis of TiO₂-Y systems by hydrothermal treatments

The TiO₂-Y combinations were created using both traditional and microwave techniques. Initially, a 1 wt.% solution of titanium(IV) chloride was prepared in distilled water with an ice-water bath. Then, 100 cm³ of the TiCl₄ solution was moved to an IKA reactor (Ika Werke GmbH, Germany), and 1 g of urea was added with continuous stirring for 15 min. The resulting solution was then shifted to a hydrothermal reactor (Parr Instrument Co., USA) or a microwave reactor (CEM Discover SPD 80, USA) for heat treatment. In the hydrothermal approach, the heat treatment settings were adjusted to T = 200 °C and t = 12 h, whereas in the microwave treatment, the settings were T = 200 °C, t = 1 min, and P = 300 W. After the process, the reactor was allowed to cool to room temperature, and the resulting substance was washed thrice with deionized water before being dried at 60 °C for 6 h.

To generate the TiO₂-Y systems, the procedure started by dissolving 50 mg of YCl₃·6H₂O (for 1 wt.% yttrium) and 100 mg of urea in 100 cm³ of water, which was then placed in the IKA reactor (Ika Werke GmbH, Germany). Simultaneously, a suspension of pre-synthesized TiO₂ in water (1 g of TiO₂ in 100 cm³) was prepared. The TiO₂ suspension was combined with the yttrium precursor solution and stirred for 30 min to ensure uniformity. The resulting mixture underwent hydrothermal microwave treatment, with the following heat treatment conditions applied: T = 200 °C, t = 12 h for a conventional hydrothermal process; T = 200 °C, t = 5 min, P = 300 W for microwave treatment. After the process was completed, the reactor was allowed to cool to room temperature, and the resulting material was washed three times with deionized water. Subsequently, it was dried at 60 °C for 6 h. Each set of synthesized samples was labeled using the formula mentioned below:

$$\text{Method abbreviation}_X\%Y, \quad (1)$$

where *Method abbreviation*—M in case the microwave processing; H—for a conventional hydrothermal treatment, *X%*—the amount of yttrium (wt.% Y = 0.25, 0.5, 1, 1.5, and 2).

Characterization of TiO₂-Y systems

The physicochemical characterization of the fabricated TiO₂-Y systems included the crystalline structure (X-ray diffraction—XRD), BET measurement (low-temperature N₂ sorption), X-ray photoelectron spectroscopy (XPS), morphology (transmission electron microscopy—TEM), surface composition (energy dispersive X-ray analysis—EDX) and optical properties (diffuse reflectance spectroscopy—DRS and photoluminescence—PL). The detailed data on the conducted physicochemical analyses are presented in Supplementary Materials.

Photocatalytic activity

Light sources

This study utilized a UV light emission diode (LED) light source that made use of LED strips emitting light at a wavelength of 395 nm. Specifically, a 5050 SMD low-voltage LED strip from MEiSSA, Poland, featuring 60 LEDs per meter and generating 7.2 W per meter, was employed in the construction of the reactor. To achieve a power output of 10 W, a 1.5-m length of the same LED strip was used. The LED strip was positioned within an aluminum radiator, accompanied by a fan connected to an IoT thermoregulator, ensuring consistent experimental conditions. The entire setup was linked to a ballast manufactured by Mean-Well, Taiwan, with the power output being verified to align with the intended value.

Photo-oxidation test

To begin the experiment, a solution of carbamazepine was prepared by dissolving 20 mg of CBZ in 1 dm³ of water. For each experimental iteration, 100 cm³ of the prepared CBZ solution was utilized. This solution was then mixed with 100 mg of photocatalyst in a photoreactor. To minimize the impact of ambient light, the entire process was conducted within a dark enclosure. The resulting mixture was thoroughly stirred without exposure to light for 30 min to establish adsorption/desorption equilibrium. Subsequently, the UV-LED lamp was switched on, and the reaction mixture was exposed to irradiation. At regular intervals of 30 min (up to a total of 240 min, after which irradiation was stopped), a 3 cm³ portion of the suspension was collected and filtered using a syringe filter manufactured by Macherey–Nagel in Germany. The filtered solution was then analyzed using a UV–Vis spectrophotometer (Shimadzu UV 2020, Japan) across the wavelength range of 200–700 nm, with the spectrum of demineralized water serving as the reference baseline. The maximum absorbance of the pollutant was observed at a wavelength of 265 nm. To determine the photocatalytic activity of the samples, the calibration curve method was employed, using the equation $y = 0.0341x + 0.0139$, where x represented the CBZ concentration and y denoted the maximum absorbance value.

Kinetic study

The kinetics of CBZ photooxidation were assessed using a pseudo-first-order kinetic model. This model postulates that the degradation rate is directly proportional to the surface coverage (θ) of CBZ, expressed as follows:

$$r = \frac{dC}{dt} = k\theta = \frac{kKC_0}{1 + KC_0 + K_s C_s} \quad (2)$$

Here, k represents the reaction rate constant, ' θ ' denotes the surface coverage by CBZ, K and K_s are the adsorption coefficients for CBZ and water, respectively, C_0 stands for the initial concentration of CBZ, and C_s represents the concentration of water. The concentration of water, C_s remains nearly constant and is significantly higher than the concentration of CBZ. Consequently, we can express Eq. (3) in the following form:

$$\ln \frac{C_t}{C_0} = -k_1 t \quad (3)$$

In Eq. (3), k_1 signifies the first-order rate constant, and t is the time of irradiation.

Verification of the degradation mechanism using scavengers

The study aimed to comprehend the role of charge carriers and reactive oxygen species in the photocatalytic reaction, providing insights into the mechanism of degradation of organic contaminants in the presence of the synthesized TiO₂-Y systems. To evaluate the photocatalytic activity, the method described in section “**Photo-oxidation test**” was employed, with the introduction of scavenger solutions in appropriate quantities. The concentrations of the scavenger solutions were adjusted to achieve a level of 20 mg/dm³ for CBZ. Specifically, ammonium oxalate was selected as the scavenger for holes (h⁺), AgNO₃ for electrons (e⁻), tert-butyl alcohol for free hydroxyl radicals ([•]OH), and benzoquinone for superoxide radical anions ([•]O₂⁻).

MS measurement

To better identify the byproducts resulting from the photocatalytic oxidation of cbz using variously prepared TiO₂-Y samples, we conducted MS measurements. The ESI–MS spectra were acquired using a Bruker amaZon SL ion trap instrument (Germany), which was equipped with an electrospray ion source operating in infusion mode. The sample solution was introduced into the ionization source at a flow rate of 5 μ L min⁻¹ via a syringe pump. The instrument operated in the *enhanced resolution mode* within a mass range of 50–30,000 m/z, scanning at a rate of 8100 m/z per second. The capillary voltage was set to +4.5 kV, with an endplate offset of -500 V. The ion source temperature was maintained at 80 °C, while the desolvation temperature was set to 250 °C. Nitrogen served as the cone gas, and helium as the desolvating gas, with flow rates of 800 L h⁻¹ and 50 L h⁻¹, respectively. The mass spectrometer was operated in both positive and negative ionization modes.

Results and discussion

Characterization of yttrium-doped TiO₂ systems

Figure 1 illustrates the XRD patterns of pure and yttrium-doped titanium dioxide systems synthesized through conventional and microwave hydrothermal pathways. The indexed peaks indicate that all analyzed systems exhibit an anatase tetragonal structure with a space group of I_{41}/amd , which closely matches the International Centre for Diffraction Data (ICDD) 9015929 card³⁰. The absence of additional crystal phases and shifts in XRD patterns

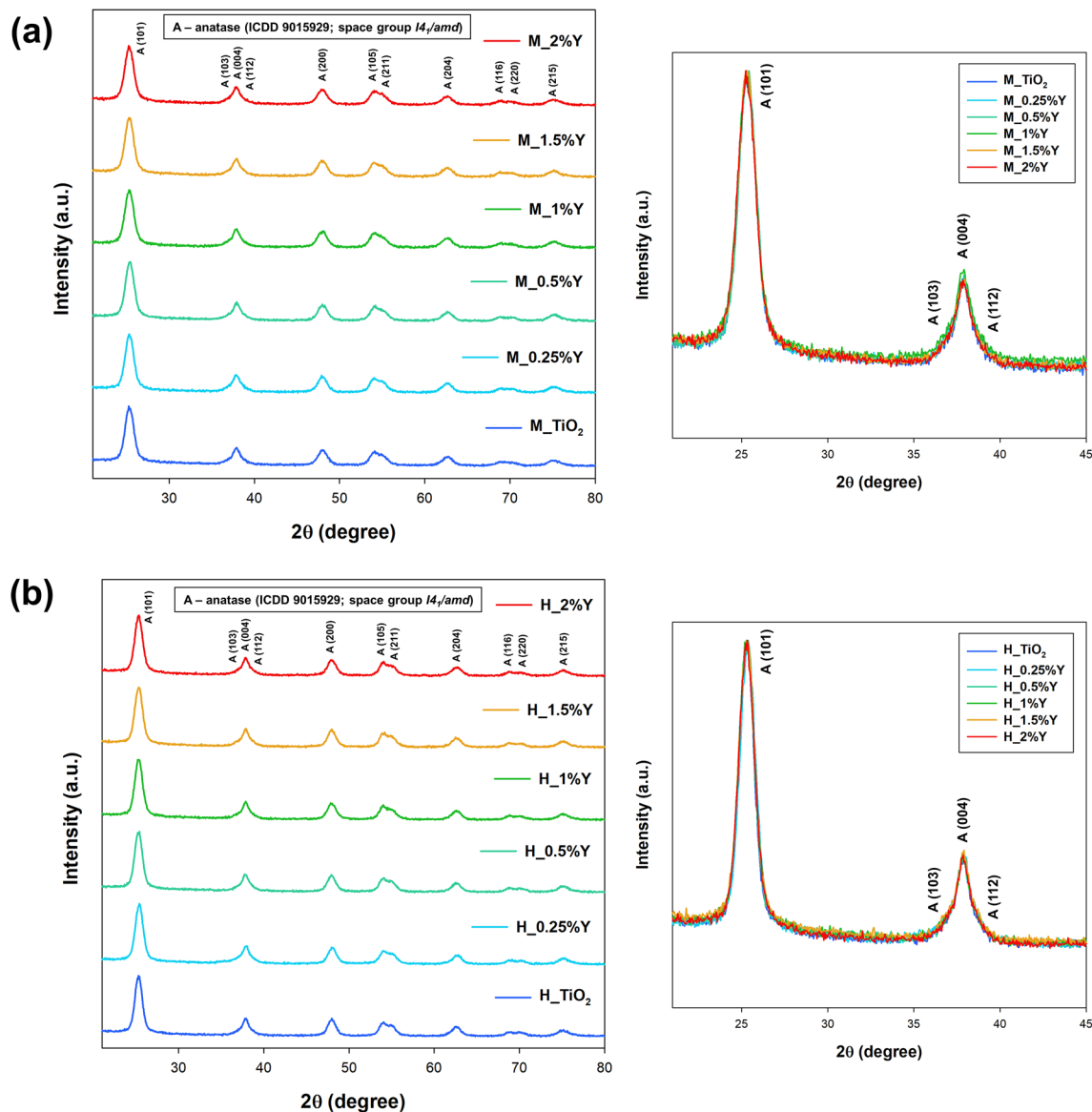


Figure 1. The XRD patterns for TiO₂-Y systems synthesized by (a) microwave and (b) conventional treatments.

confirms the fabrication of pure anatase structure samples. The larger ion radius of Y³⁺ (0.90 Å) compared to Ti⁴⁺ (0.61 Å) makes it challenging for Y³⁺ to enter the TiO₂ lattice³¹. Additionally, the low content and high dispersity of Y species contribute to the absence of extra peaks, such as the oxide form of yttrium³². To determine the structural properties of the samples, Rietveld analysis was conducted using FullProf software, and the results for selected systems are presented in Fig. S1 of the Supplementary Materials. The crystallite size (D) was determined using the Scherrer equation (Eq. 1 is presented in the Supplementary Materials) and the corresponding values for all samples are compiled in Table 1. In the context of conventional hydrothermal treatment, no noteworthy distinctions were discerned in the mean crystallite size between the yttrium-doped samples and the pure TiO₂. However, a marginal augmentation in the average crystallite size was noted with microwave processing. This increase is ascribed to the elevated kinetics inherent in microwave processes, as validated in our earlier research. Irrespective of the hydrothermal treatment method employed, the refined lattice parameters align well with those documented in the literature^{33–35}.

The parameters related to the porous structure of the synthesized TiO₂-Y systems are provided in Table 1. Additionally, the N₂ adsorption–desorption isotherms can be found in Fig. S2 of the Supplementary Materials. The isotherms exhibit type IV characteristics indicating capillary condensation in mesopores and limited uptake at high p/p_0 values^{36,37}. At low relative pressures, adsorption follows a similar to that of a non-porous adsorbent, undergoing single-layer-multilayer adsorption. Additionally, the materials exhibit an H1 hysteresis loop type, which is typical for porous materials composed of uniform particles arranged in regular arrays with narrow pore size distributions³⁸. When comparing the obtained nitrogen adsorption isotherms, no significant differences were observed between the systems synthesized using hydrothermal or microwave treatment. However, the supported yttrium systems exhibit lower BET surface areas compared to bare titanium dioxide. The reduction

Sample	D (nm)	Lattice parameters		Porous structure parameters			Energy band gap
		Anatase		A_{BET} ($\text{m}^2 \text{g}^{-1}$)	V_p ($\text{cm}^3 \text{g}^{-1}$)	Sp (nm)	E_g (eV)
a (Å)	c (Å)						
Conventional treatment							
H_TiO ₂	15.6	3.8011	5.5281	178	0.397	3.9	3.2
H_0.25%Y	15.4	3.7838	9.5095	175	0.383	4.4	3.2
H_0.5%Y	15.1	3.7778	9.4832	171	0.372	4.6	3.1
H_1%Y	15.3	3.7951	9.5201	170	0.353	4.8	3.1
H_1.5%Y	15.5	3.7962	9.5143	170	0.348	6.7	3.1
H_2%Y	15.4	3.7935	9.5137	168	0.344	6.8	3.1
Microwave treatment							
M_TiO ₂	15.2	3.7907	9.5050	222	0.376	3.7	3.2
M_0.25%Y	15.5	3.7942	9.5151	214	0.365	4.2	3.2
M_0.5%Y	15.7	3.8081	9.5443	214	0.358	4.2	3.1
M_1%Y	16.1	3.7943	9.5145	212	0.349	4.7	3.1
M_1.5%Y	16.3	3.7891	9.5056	210	0.324	4.9	3.1
M_2%Y	16.5	3.7882	9.5044	209	0.310	4.9	3.1

Table 1. X-ray diffraction, low-temperature N₂ sorption, and diffuse reflectance spectroscopy results for yttrium-doped TiO₂ systems.

becomes more pronounced with an increase in yttrium content. Considering that the pore size of anatase ranges between 4–6 nm, it is plausible that yttrium oxide particles are not hosted within the pores but rather adsorbed on the outer surfaces of titanium dioxide. This could lead to the blocking of the porous surface, resulting in a decrease in surface area development and pore volume. Nevertheless, it is crucial to highlight that the utilization of microwave hydrothermal treatment facilitates the enhanced development of the BET surface area.

The X-ray Photoelectron Spectroscopy (XPS) technique was used to investigate the chemical composition of the surface layer (approx. 10 nm depth) in the synthesized TiO₂-Y systems. Table 2 presents the atomic composition of the detected elements, namely titanium, oxygen, and yttrium. High-resolution (HR) XPS spectra for selected systems are shown in Fig. 2.

It is crucial to highlight a notable difference in the atomic content of yttrium among the acquired TiO₂-Y systems. The atomic content of yttrium in the microwave-synthesized samples closely aligns with the expected values, whereas in the hydrothermal method, the concentrations are lower than anticipated. Furthermore, the hydrothermal method exhibits lower atomic fractions of oxygen, correlating well with the diminished yttrium content, given that yttrium is present in an oxidized form in the synthesized materials. These findings suggest that the swift microwave method effectively facilitates the doping of TiO₂ with rare earth metals.

Two distinct peaks were observed in the Ti 2p region with binding energies centered at 458.5 eV and 464.2 eV, corresponding to Ti 2p_{3/2} and Ti 2p_{1/2}, respectively^{39,40}. The splitting difference of 5.7 eV between these two bands indicates the presence of Ti⁴⁺ in the sample⁴¹. The absence of any energy shift in the Ti 2p peaks confirms that yttrium doping occurs only as a surface modification, without incorporating yttrium ions into the anatase lattice structure.

The O 1s peaks observed at 523.0 eV and 531.5 eV were assigned to lattice oxygen and hydroxyl groups, respectively⁴². It is noteworthy that an increase in yttrium concentration results in a higher oxygen content derived from hydroxyl groups. Additionally, literature reports suggest that these hydroxyl groups can react with photoinduced holes, generating highly oxidizing surface-bound hydroxyl radicals⁴³. It is important to mention

Sample	Content (at.%)		
	Ti 2p	O 1s	Y 3d
Conventional treatment			
H_0.25%Y	33.5	66.3	0.2
H_1%Y	31.8	67.4	0.8
H_2%Y	30.6	67.8	1.6
Microwave treatment			
M_0.5%Y	33.6	66.0	0.4
M_1%Y	31.5	67.4	1.1
M_2%Y	29.7	68.2	2.1

Table 2. XPS analysis of Ti, O, Y content (at.%) for the synthesized materials.

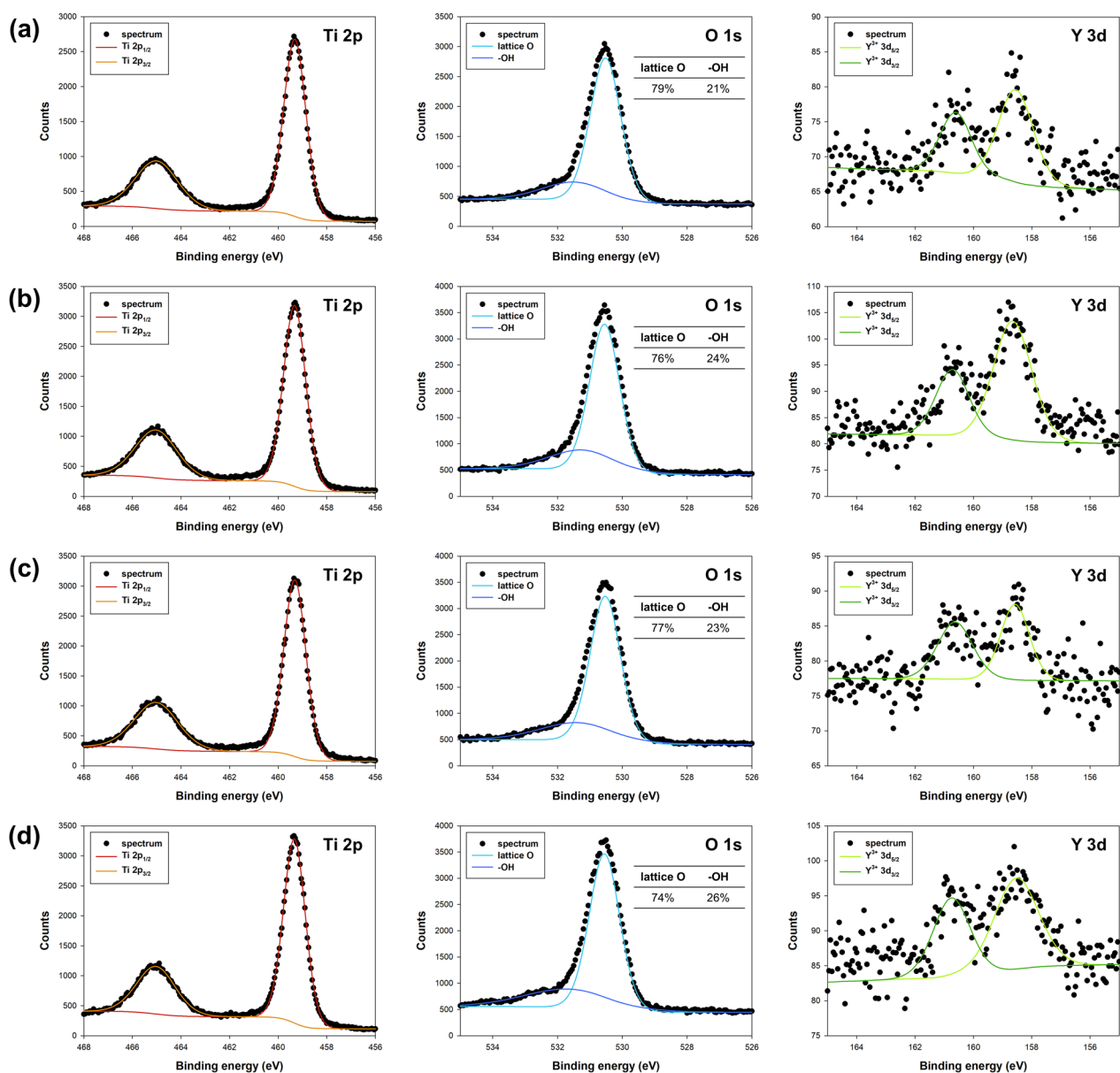


Figure 2. XPS spectra of Ti 2p, O 1 s, and Y 3d regions for (a) H_1%Y, (b) H_2%Y, (c) M_1%Y, and (d) M_2%Y.

that, in all analyzed systems, the concentration of hydroxyl groups is higher in materials obtained using microwave hydrothermal treatment.

The binding energy values of Y 3d_{5/2} and Y 3d_{3/2} for the TiO₂-Y systems are approximately 158.5 eV and 160.5 eV, respectively, with a spin-orbit splitting of 2 eV^{44–46}. These results provide evidence that the oxidation state of yttrium ions is predominantly trivalent.

A TEM study was conducted to explore the impact of yttrium doping on the morphology of anatase, as illustrated in Fig. 3. The average particle size of the nanoparticles (NPs) is 20–25 nm, displaying a regular shape characteristic of bare anatase. However, unlike the regular structure observed in samples with lower yttrium content (e.g., 0.25% and 0.5 wt.% Y), the presence of 1% and 2% wt. Y results in NPs with more irregular particle edges. This irregularity is particularly pronounced in materials obtained through the microwave pathway. These irregular structures were also described by Bingxin Zhao et al.³⁴, who highlighted their role in facilitating the diffusion of photoinduced electrons. The selected area electron diffraction (SAED) patterns, shown in the insets for all analyzed systems, clearly indicate the presence of polycrystalline circles in the anatase phase^{47,48}. Figure S3 (see Supplementary Materials) presents the TEM d-spacing profile, demonstrating that the (101) planes did not experience expansion due to yttrium doping. This finding aligns well with the calculated interplanar distance (101) based on the diffraction angle, confirming that yttrium ions have not entered the TiO₂ lattice⁴⁹.

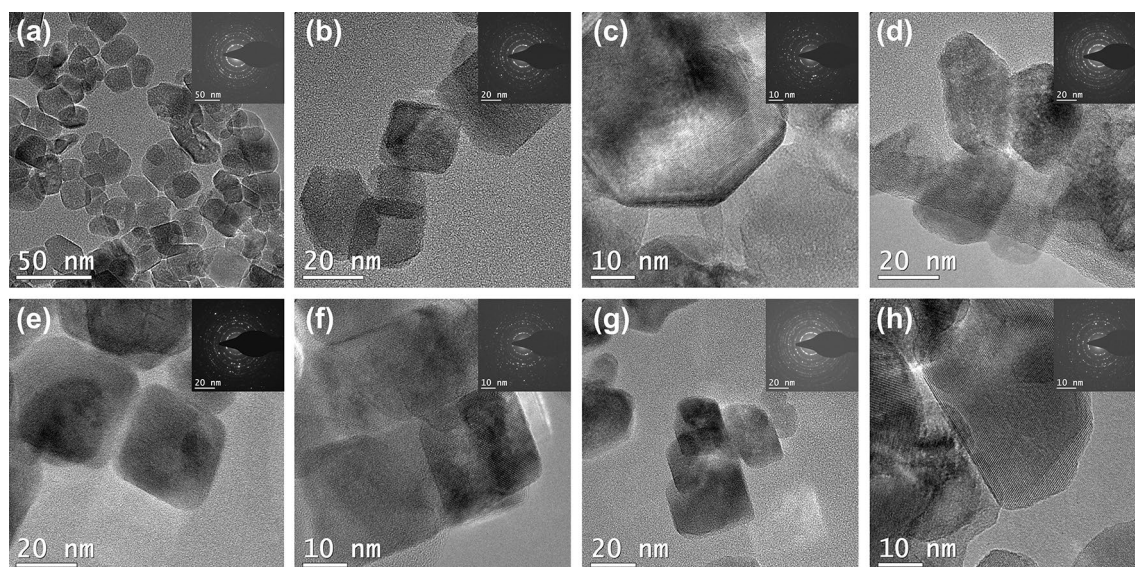


Figure 3. TEM images of: (a) H_0.25%Y, (b) H_0.5%Y, (c) H_1%Y, (d) H_2%Y, (e) M_0.25%Y, (f) M_0.5%Y, (g) M_1%Y, and (h) M_2%Y. SAED patterns are shown in the inset.

Additionally, it should be noted that, in the case of TiO_2 -Y systems, no significant changes in sample morphology were observed based on the type of hydrothermal treatment used, whether conventional or microwave.

The EDX results and elemental mapping, depicted in Fig. S4 in the Supplementary Materials, highlight the presence of three main elements in the synthesized systems: titanium, oxygen, and yttrium. Importantly, the distribution of yttrium is uniform across the entire sample area in all analyzed materials. Furthermore, it is noteworthy that the EDX results (refer to Table S1 in the Supplementary Materials) corroborate the earlier conclusions drawn from the XPS analysis. They confirm that the microwave method is more effective than the hydrothermal method in the yttrium doping process, resulting in a higher weight percentage of yttrium in systems obtained by the microwave route.

Photocatalytic ability

In order to investigate the optical response of TiO_2 -Y systems, UV-Visible diffuse reflectance spectra were conducted. The DRS spectra of Y-doped TiO_2 systems synthesized through various hydrothermal routes are shown in Fig. S5 (refer to Supplementary Materials). Compared to bare TiO_2 , the optical absorption edges of TiO_2 -Y systems exhibited a red shift, particularly in materials with lower weight percentages of yttrium ions. This shift in the optical absorption band can be attributed to the presence of Y ions on the surface of TiO_2 , potentially causing a charge imbalance transition between the Y 3d electrons and the conduction or valence electrons of the pure TiO_2 . The creation of dopant levels near the conduction band can explain the red shift in the band gap. To determine the optical band gaps, the diffuse reflectance (R) of both the undoped and TiO_2 -Y systems can be correlated to the Kubelka-Munk function. The calculated band gaps were approximately 3.2 eV for bare TiO_2 and 3.1 eV for yttrium-doped TiO_2 systems. Niu et al.⁵⁰ previously reported a red shift in the band gap of Y-doped TiO_2 nanoparticles, attributed to charge transfer between the f electrons of Y^{3+} and the TiO_2 conduction or valence band, as observed through diffuse reflectance studies. Muktaridha et al.⁵¹ also reported a blue shift in the band gap of Y-doped systems using UV-Visible absorption studies. This blue shift was explained by the occupied states of Ti 3d and the up-shift of the Fermi level. The reason for these blue shifts was the gradual movement of the conduction band due to dopant incorporation, which is not observed in the present study.

The room-temperature photoluminescence (PL) (Fig. 4) spectra exhibit a distinctive broad and intense emission band around 450 nm, characteristic of pure TiO_2 ⁵². The shape of the spectra indicates that the presence of yttrium does not introduce any new photoluminescence features. Previous studies on titanium dioxide emissions have identified two primary peaks at approximately 396 nm and 462 nm, corresponding to energy levels of 3.13 eV and 2.68 eV, respectively^{53,54}. However, a broader luminescence band has also been observed, resulting from merging these two narrow peaks. These peaks are associated with the bandgap and charge-transfer transitions from Ti^{3+} to oxygen anions in a TiO_6^{8-} complex. Interestingly, regardless of the materials analyzed, there is a noticeable emission suppression in TiO_2 -Y systems, indicating hindered recombination of photogenerated holes and electrons^{54,55}. The presence of yttrium ions introduces additional electron transport pathways, facilitating faster separation and efficient transport of photogenerated charge carriers. This enhanced charge carrier mobility contributes to reduced recombination rates and suppressed photoluminescence emission in yttrium-doped TiO_2 . In yttrium-doped systems, the introduction of more traps into TiO_2 and the trapping of additional photoelectrons prevent recombination, resulting in reduced photoluminescence emission intensity. However, it is important to note that an increase in luminescence has been observed with higher yttrium content. This effect can be attributed to the modification of charge carrier dynamics by the high yttrium concentration, leading to a more significant population of excited states^{56,57}. As a result, there is a higher emission intensity upon

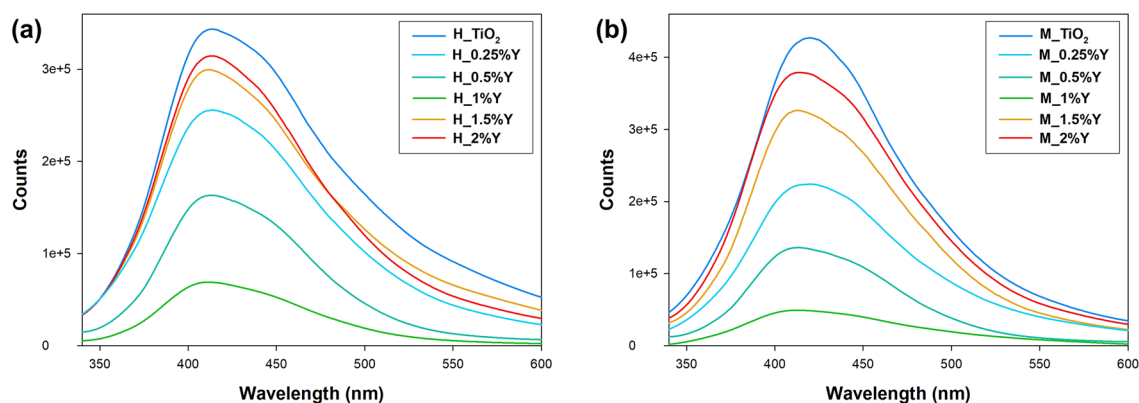


Figure 4. The PL spectra for TiO₂-Y systems synthesized by (a) conventional and (b) microwave treatments.

excitation. Furthermore, the choice of hydrothermal synthesis route impacts the efficiency of photoluminescence. The conventional method yields a higher luminescence yield, likely due to the lower yttrium content in these materials. On the other hand, as previously mentioned, the microwave method allows for effective doping of TiO₂ with rare earth metals, leading to better quenching of luminescence and, consequently, more efficient separation of charge carriers.

The crucial point of the research was to determine the effectiveness of the fabricated TiO₂-Y systems in removing harmful carbamazepine waste through the photooxidation process. The collected degradation curves are presented in Fig. 5.

Under UV-LED light irradiation, CBZ degradation in the presence of TiO₂ was at a low level, amounting to 60% and 70% of the efficiency for conventional and microwave processing, respectively. Doping bare TiO₂ with small amounts of yttrium ions (0.25–1 wt.% Y) significantly improved photocatalytic activity. Almost all of the CBZ was removed (91% and 96% for conventional and microwave treatment, respectively) when the yttrium concentration was 1 wt.%. This enhanced photocatalytic activity was attributed to the efficient junctions between yttrium ions and the surface of TiO₂. The interaction of dopant ions with the semiconductor's surface increased light absorbance and boosted carrier transfer. However, excessive yttrium dopants may act as recombination centers for carriers and hinder light absorption^{58,59}. Consequently, the photo-oxidation efficiency of CBZ decreases to 66% and 73% for conventional and microwave treatment, respectively, when the systems contain 2 wt.% of yttrium.

It should be noted that changing the hydrothermal treatment method impacts the photocatalytic performance of yttrium-doped TiO₂ systems. Regardless of the specific system analyzed, samples produced using the microwave method exhibited increased efficiency in removing CBZ. Several factors contribute to this observation. While the doping process did not alter the electronic structure of TiO₂, it did enhance the absorption of UV radiation, as indicated by the calculation of bandgap energy. Moreover, the presented photoluminescence spectra demonstrated improved luminescence quenching for systems obtained through the microwave pathway, indicating a more effective transfer of electron-hole charge carriers. Additionally, it is worth emphasizing that materials prepared using microwave radiation show higher surface area development, a critical parameter in the photo-oxidation process. Furthermore, microwave processing resulted in a larger average crystallite size and facilitated the attainment of desired levels of yttrium on the surface of bare TiO₂. Altogether, these factors collectively contributed to the observed enhancement in the photocatalytic performance of TiO₂-Y systems synthesized using the microwave method.

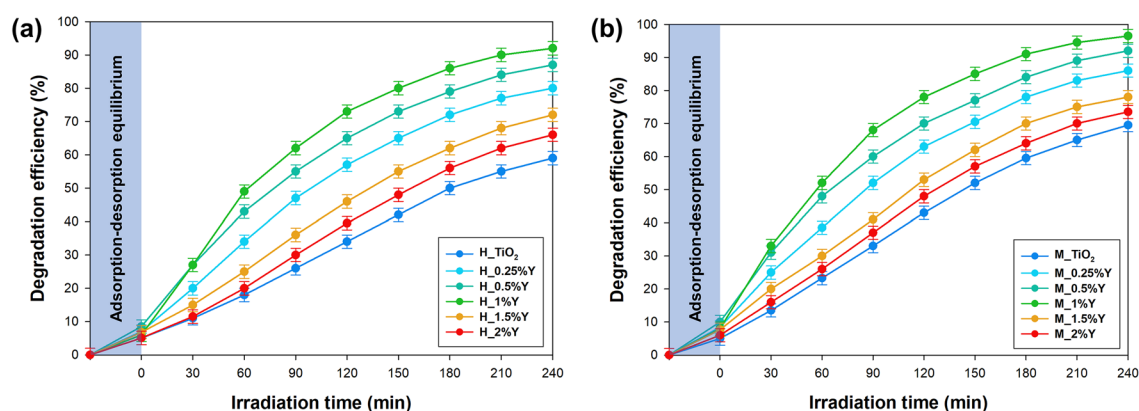


Figure 5. The efficiency of carbamazepine photo-oxidation using TiO₂-Y systems synthesized by (a) conventional and (b) microwave treatments.

The revised Langmuir–Hinshelwood model provides a suitable framework for elucidating the degradation mechanism, aligning with the surface reaction concept frequently examined in existing literature^{60–62}. To determine the rate constant parameter, the sorption process was intentionally omitted from the calculations. In accordance with Eqs. (2) and (3), the apparent values of parameter k_1 for each catalyst were computed by analyzing the slope of the $\ln(C_t/C_0)$ vs. time plot. The calculated values are presented in Table S2, available in the Supplementary Materials for comparison. Consistent with previously presented results, among a series of materials, the M_1%Y catalyst exhibits the highest reaction rate constant at 0.0135 min⁻¹. In contrast, the material obtained through the conventional hydrothermal method showed a consistent reaction rate of 0.0108 min⁻¹ – H_1%Y. Significantly, regardless of the series of materials analyzed, transitioning from the microwave treatment method to the conventional hydrothermal technique consistently results in a decrease in the reaction rate constant. This reduction can be primarily attributed to an increased recombination rate and diminished absorption of UV light.

Table 3 shows the current state of knowledge in the field of photocatalytic degradation of carbamazepine.

The presented data underscores the importance of addressing the challenge of carbamazepine removal through photocatalysis, as evidenced by extensive research within the scientific community. A thorough analysis of existing scientific literature reveals a common reliance on photocatalytic water purification systems with ultraviolet light sources. The duration of the photocatalytic process is intricately linked to factors such as CBZ concentration and the type and quantity of the photocatalyst used. It is crucial to note that certain referenced studies still employ gas discharge lamps, a practice inconsistent with the principles of green chemistry and sustainable development. In this context, our study's results, based on the implementation of an LED solution, seem to align more closely with the expectations of the scientific community. The achieved photoactivity with the M_1%Y catalyst notably corresponds with values documented in the prevailing scientific literature. Furthermore, the adoption of the LED system has the potential to reduce electricity demand, a factor we previously addressed in our research^{70,71}.

For the reusability test, the photocatalysts H_1%Y and M_1%Y were chosen. Five consecutive cycles of CBZ photo-oxidation were carried out to evaluate their photocatalytic reusability, as shown in Fig. S6 of the Supplementary Materials. After each cycle, the photocatalyst was separated from the reaction suspension through filtration and reused without any additional treatment. The results showed that the efficiency of photocatalytic degradation decreased by approximately 10% after the 5th cycle compared to the 1st cycle. This slight decline in activity after each irradiation cycle could be attributed to the loss of photocatalysts during the separation process.

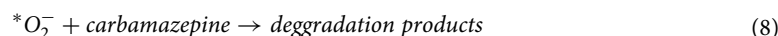
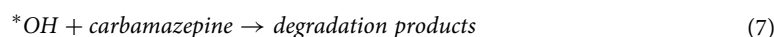
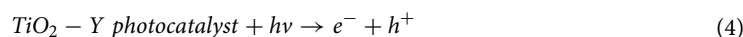
The FTIR spectra of the TiO₂-Y samples (Fig. S7, Supplementary Materials) showed no significant difference between the samples before and after the CBZ photo-oxidation process. Prior to irradiation, the spectra exhibited stretching vibrations of Ti–O bonds (800–900 cm⁻¹)⁷² and surface hydroxyl groups (1625 cm⁻¹ and 3430 cm⁻¹)^{73,74} in the mentioned systems. However, no additional bands were observed after the CBZ photo-oxidation process in the TiO₂-Y systems. The only noticeable change was a decrease in the intensity of bands originating from the surface hydroxyl groups^{75,76}. These spectra confirm that there is minimal alteration to the surface of the analyzed photocatalysts, which is consistent with the results obtained from the previous reusability tests.

Figure S8 (see Supplementary Materials) shows the data obtained by introducing scavengers into the CBZ solution to explore the degradation mechanism in yttrium-doped TiO₂ systems. These scavengers were intended to capture the photo-generated electrons, holes, and primary reactive oxygen species such as [•]OH and [•]O₂⁻. The efficiency of CBZ photooxidation decreased by approximately 20% upon the introduction of ammonium oxalate and silver nitrate, which acted as scavengers for electrons and holes. The reason for only a slight decrease in CBZ removal efficiency can be due to the enhanced separation of charge carriers facilitated by the presence of yttrium ions on the TiO₂ surface^{77,78}. This effect was confirmed by analyzing the photoluminescence spectra. Furthermore, the addition of *tert*-butanol, a scavenger for hydroxyl radicals ([•]OH), significantly decreased the photodegradation efficiency, reducing it by approximately 51% for the analyzed materials. This suggests that [•]OH is an active species involved in the photo-oxidation process. On the other hand, the scavenging of superoxide radical anions ([•]O₂⁻) considerably impacted the efficiency of CBZ removal. In the case of the analyzed samples, it led to a decrease in efficiency of 26% and 20% for M_1%Y and H_1%Y, respectively. This indicates that [•]O₂⁻ plays a crucial role in the photocatalytic degradation mechanism. Based on these findings, it can be inferred that the mechanisms occurring in the aquatic environment are primarily governed by the generation of reactive oxygen

Sample	CBZ concentration (mg/dm ³)	Amount of photocatalyst (g/dm ³)	Degradation efficiency (%)	Irradiation time (min)	Parameters of the light source	Refs.
M_1%Y	20	1	95	240	UV-LED (395 nm)	This work
g-C ₃ N ₄ /TiO ₂	10	1	72	360	UV-A lamp 24 W	63
Fe ₃ O ₄ @SiO ₂ /d-TiO ₂ -Pt + H ₂ O ₂	14	0.5	95	120	Xe-lamp 300W	64
P25	10	1	70	120	Xe-lamp 1000W	65
Ag ₃ PO ₄ /GO	5	0.5	99	120	PCX50C Discover (420 nm)	66
TiO ₂	10	1.5	99	120	UV-A (365 nm)	67
graphene oxide/TiO ₂	10	0.5	99	90	Hg-lamp (125W)	68
TiO ₂ /Ti ₃ C ₂ T _x	5	0.5	98	180	Solar simulator	69

Table 3. Summary of literature data on the degradation of carbamazepine.

species (ROS), including hydroxyl radicals and superoxide radical anions^{79,80}. The major steps in the photocatalytic mechanism are illustrated in the equations below.



The products of CBZ photodegradation were detected using the MS technique and identified based on their mass spectra. The resulting mass spectra are shown in Table S3 in the Supplementary Materials. Figure S9 (see in Supplementary Materials) illustrates the mechanism of by-product formation, which is further discussed compared to existing literature. During the photocatalytic degradation of CBZ, two primary pathways are observed. Hydroxyl radical dot radicals, generated during the photocatalytic process, attack the aromatic ring of CBZ, resulting in the formation of C1 (monohydroxy CBZ, $m/z = 253$)^{81,82}. The subsequent addition of another hydroxyl radical leads to the formation of C2 (dihydroxy CBZ, $m/z = 265$)⁸³. The by-product at C3 ($m/z = 238$) is formed through a combination of ring contraction and reduction (-CONH₂) of (1,1(1-aminovinyl)-10,10a-dihydroacridine-9-carbaldehyde)⁸³. Further degradation of the intermediate product C3 via oxidation yields C4 (acridine, $m/z = 180$), while the transformation products C5 (2-hydroxy acridine-9-carboxaldehyde, $m/z = 224$) and C6 (formaldehyde-acridine (1/1), $m/z = 195$) are also likely to be present⁸⁴. Finally, these intermediate products undergo an additional ring-opening reaction, resulting in the production of acetic acid, which can be mineralized into CO₂ and H₂O through oxidation.

Conclusions

The findings presented in this study underscore the remarkable enhancement of yttrium-doped TiO₂'s photocatalytic activity for CBZ degradation under UV-LED light irradiation. The introduction of small quantities of yttrium ions (0.25–1 wt.%) resulted in a substantial improvement in photocatalytic efficiency, culminating in nearly complete CBZ removal at a yttrium concentration of 1 wt.%. This augmented performance can be attributed to the formation of efficient junctions between yttrium ions and the TiO₂ surface, amplifying light absorption and carrier transfer processes. Notably, the choice of hydrothermal treatment method played a pivotal role in influencing the photocatalytic efficacy of yttrium-doped TiO₂ systems. Microwave-assisted hydrothermal synthesis exhibited a superior capacity for CBZ removal when compared to conventional hydrothermal techniques. This superiority arises from several factors, including heightened light absorption, more efficient charge carrier transfer, expanded surface area, and increased average crystallite size achieved through microwave processing.

Furthermore, the examination of scavengers unveiled the involvement of reactive oxygen species (ROS), including hydroxyl radicals ([•]OH) and superoxide radical anions ([•]O²⁻) in the photocatalytic degradation mechanism. The introduction of scavengers led to a reduction in the efficiency of CBZ removal, underscoring the significance of these species in the degradation process. Collectively, this study offers valuable insights into the utilization of microwave technology in yttrium-doped TiO₂ fabrication, shedding light on its substantial influence on photocatalytic performance. It highlights the potential of microwaves as an innovative and eco-friendly synthesis technique, exemplified through the enhanced photocatalysis of yttrium-doped TiO₂. However, it is essential to acknowledge that a comprehensive understanding of the underlying mechanisms remains a critical stepping stone towards fully harnessing the environmental and economic benefits of this approach.

Data availability

The data that support the findings of this research are available from the corresponding author upon reasonable request.

Received: 6 November 2023; Accepted: 30 December 2023

Published online: 02 January 2024

References

1. Ma, Y. *et al.* Titanium dioxide-based nanomaterials for photocatalytic fuel generations. *Chem. Rev.* **114**, 9987–10043 (2014).
2. Gupta, S. M. & Tripathi, M. A review of TiO₂ nanoparticles. *Chin. Sci. Bull.* **56**, 1639–1657 (2011).
3. Hoffmann, M. R., Martin, S. T., Choi, W. & Bahnemann, D. W. Environmental applications of semiconductor photocatalysis. *Chem. Rev.* **95**, 69–96 (1995).
4. Fox, M. A. & Dulay, M. T. Heterogeneous photocatalysis. *Chem. Rev.* **93**, 341–357 (1993).
5. Innocenzi, V., De Michelis, I., Kopacek, B. & Vegliò, F. Yttrium recovery from primary and secondary sources: A review of main hydrometallurgical processes. *Waste Manag.* **34**, 1237–1250 (2014).
6. Liu, K. *et al.* A green yttrium extraction system containing naphthenic acid, trioctyl/decylamine and isopropanol. *J. Clean. Prod.* **415**, 137747 (2023).
7. Innocenzi, V., De Michelis, I., Ferella, F. & Vegliò, F. Secondary yttrium from spent fluorescent lamps: Recovery by leaching and solvent extraction. *Int. J. Miner. Process.* **168**, 87–94 (2017).
8. Zhang, X. *et al.* Yttrium separation by phosphorylcarboxylic acid and the underlying tetrad effect along lanthanide unveiled from different microscopic interactions. *Fundam. Res.* (2023, in press).

9. Li, D. A review on yttrium solvent extraction chemistry and separation process. *J. Rare Earths*. **35**, 107–119 (2017).
10. Haider, A. J., Jameel, Z. N. & Al-Hussaini, I. H. M. Review on: Titanium dioxide applications. *Energy Procedia* **157**, 17–29 (2019).
11. Siddhartha, S., Patnaik, A. & Bhatt, A. D. Mechanical and dry sliding wear characterization of epoxy-TiO₂ particulate filled functionally graded composites materials using Taguchi design of experiment. *Mater. Des.* **32**, 615–627 (2011).
12. Fang, W. Q. *et al.* Hierarchical structures of single-crystalline anatase TiO₂ nanosheets dominated by 001 facets. *Chem. Eur. J.* **17**, 1423–1427 (2011).
13. Nasir, M. *et al.* Characterization and activity of the Ce and N co-doped TiO₂ prepared through hydrothermal method. *Chem. Eng. J.* **236**, 388–397 (2014).
14. Khan, I. *et al.* Green synthesis of SrO bridged LaFeO₃/g-C₃N₄ nanocomposites for CO₂ conversion and bisphenol A degradation with new insights into mechanism. *Environ. Res.* **207**, 112650 (2022).
15. Khan, I. *et al.* Efficient CO₂ conversion and organic pollutants degradation over Sm³⁺ doped and rutile TiO₂ nanorods decorated-GdFeO₃ nanorods. *Int. J. Hydrog. Energy*. **48**, 32756–32770 (2023).
16. Zaman, S. *et al.* Synthesis of mediator free hollow BiFeO₃ spheres/porous g-C₃N₄ Z-scheme photocatalysts for CO₂ conversion and Alizarin Red S degradation. *Mater. Sci. Semicond. Process.* **162**, 107534 (2023).
17. Bavykin, D. V., Parmon, V. N., Lapkin, A. A. & Walsh, F. C. The effect of hydrothermal conditions on the mesoporous structure of TiO₂ nanotubes. *J. Mater. Chem.* **14**, 3370–3377 (2004).
18. Sikhwihilu, L. M., Mpelane, S., Moloto, N. & Sinha Ray, S. Hydrothermal synthesis of TiO₂ nanotubes: Microwave heating versus conventional heating. In *Nanostructured Materials and Nanotechnology IV: Ceramic Engineering and Science Proceedings* (eds Mathur, S. *et al.*) 45–49 (The American Ceramic Society, 2010).
19. Ferrari, A. *et al.* Microwave-assisted superheating and/or microwave-specific superboiling (nucleation-limited boiling) of liquids occurs under certain conditions but is mitigated by stirring. *Molecules* **20**, 21672–21680 (2015).
20. Kubiak, A. *et al.* Controlled microwave-assisted and pH-affected growth of ZnO structures and their photocatalytic performance. *Powder Technol.* **386**, 221–235 (2021).
21. Samriti, X., Tyagi, R., Ruzimuradov, O. & Prakash, J. Fabrication methods and mechanisms for designing highly-efficient photocatalysts for energy and environmental applications. *Mater. Chem. Phys.* **307**, 128108 (2023).
22. Liu, N., Chen, X., Zhang, J. & Schwank, J. W. A review on TiO₂-based nanotubes synthesized via hydrothermal method: Formation mechanism, structure modification, and photocatalytic applications. *Catal. Today* **225**, 34–51 (2014).
23. Rosana, M. R., Tao, Y., Stiegman, A. E. & Dudley, G. B. On the rational design of microwave-actuated organic reactions. *Chem. Sci.* **3**, 1240–1244 (2012).
24. de la Hoz, A., Díaz-Ortiz, A. & Moreno, A. Microwaves in organic synthesis. Thermal and non-thermal microwave effects. *Chem. Soc. Rev.* **34**, 164–178 (2005).
25. Tsuji, M., Hashimoto, M., Nishizawa, Y., Kubokawa, M. & Tsuji, T. Microwave-assisted synthesis of metallic nanostructures in solution. *Chem. Eur. J.* **11**, 440–452 (2005).
26. Meng, L. Y., Wang, B., Ma, M. G. & Lin, K. L. The progress of microwave-assisted hydrothermal method in the synthesis of functional nanomaterials. *Mater. Today Chem.* **1–2**, 63–83 (2016).
27. Gayathri, S., Kottaisamy, M. & Ramakrishnan, V. Facile microwave-assisted synthesis of titanium dioxide decorated graphene nanocomposite for photodegradation of organic dyes. *AIP Adv.* **5**, 127219 (2015).
28. Kubiak, A. *et al.* A novel microwave-assisted strategy to fabricate multifunctional photoactive titania-based heterostructures with enhanced activity. *Mater. Res. Bull.* **147**, 111633 (2022).
29. Moloto, N., Mpelane, S., Sikhwihilu, L. M. & Sinha Ray, S. Optical and morphological properties of ZnO- and TiO₂-derived nanostructures synthesized via a microwave-assisted hydrothermal method. *Int. Int. J. Photoenergy*. **2012**, 189069 (2012).
30. Qi, K., Cheng, B., Yu, J. & Ho, W. A review on TiO₂-based Z-scheme photocatalysts. *Chin. J. Catal.* **38**, 1936–1955 (2017).
31. Qu, X. *et al.* Yttrium doped TiO₂ porous film photoanode for dye-sensitized solar cells with enhanced photovoltaic performance. *Results Phys.* **6**, 1051–1058 (2016).
32. da Silva Oliveira, L. *et al.* Emission of TiO₂:Y³⁺ and Eu³⁺ in water medium, under UV excitation and band gap theoretical calculus. *J. Lumin.* **257**, 119639 (2023).
33. Rajput, P. *et al.* Photocatalytic and antibacterial activity of Yttrium doped TiO₂ nanostructure. *Chem. Phys. Impact.* **5**, 100101 (2022).
34. Zhao, B. *et al.* The influence of yttrium dopant on the properties of anatase nanoparticles and the performance of dye-sensitized solar cells. *Phys. Chem. Chem. Phys.* **17**, 14836–14842 (2015).
35. Khan, M. & Cao, W. Preparation of Y-doped TiO₂ by hydrothermal method and investigation of its visible light photocatalytic activity by the degradation of methylene blue. *J. Mol. Catal. A Chem.* **376**, 71–77 (2013).
36. Muttakin, M., Mitra, S., Thu, K., Ito, K. & Saha, B. B. Theoretical framework to evaluate minimum desorption temperature for IUPAC classified adsorption isotherms. *Int. J. Heat. Mass. Transf.* **122**, 795–805 (2018).
37. Sing, K. S. W. *et al.* Reporting physisorption data for gas/solid systems with special reference to the determination of surface area and porosity. *Pure Appl. Chem.* **57**, 603–619 (1985).
38. Chang, B. Y. S. *et al.* Hydrothermally prepared graphene-titania nanocomposite for the solar photocatalytic degradation of methylene blue. *Desalination Water Treat.* **57**, 238–245 (2016).
39. Song, Z., Hrbek, J. & Osgood, R. Formation of TiO₂ nanoparticles by reactive-layer-assisted deposition and characterization by XPS and STM. *Nano Lett.* **5**, 1327–1332 (2005).
40. Dudziak, S. *et al.* Solvothermal growth of 0 0 1 exposed anatase nanosheets and their ability to mineralize organic pollutants. The effect of alcohol type and content on the nucleation and growth of TiO₂ nanostructures. *Appl. Surf. Sci.* **563**, 150360 (2021).
41. Vaiano, V., Sacco, O. & Sannino, D. Electric energy saving in photocatalytic removal of crystal violet dye through the simultaneous use of long-persistent blue phosphors, nitrogen-doped TiO₂ and UV-light emitting diodes. *J. Clean. Prod.* **210**, 1015–1021 (2019).
42. Noroozi, R., Gholami, M., Farzadkia, M. & Rezaei Kalantary, R. Synthesis of new hybrid composite based on TiO₂ for photocatalytic degradation of sulfamethoxazole and pharmaceutical wastewater, optimization, performance, and reaction mechanism studies. *Environ. Sci. Pollut. Res.* **29**, 56403–56418 (2022).
43. Dozzi, M. V., Montalbano, M., Marra, G., Mino, L. & Selli, E. Effects of anatase TiO₂ morphology and surface fluorination on environmentally relevant photocatalytic reduction and oxidation reactions. *Mater. Today Chem.* **22**, 100624 (2021).
44. Zhang, B. *et al.* Y-doped TiO₂ coating with superior bioactivity and antibacterial property prepared via plasma electrolytic oxidation. *Mater. Des.* **192**, 108758 (2020).
45. Iogo, G. M., Paparazzo, E., Nazionale delle Ricerche, C., le AldoMoro, P. Z. & Zacchetti, I. N. XPS studies on cerium, zirconium and yttrium valence states in plasma-sprayed coatings. *Surf. Interface Anal.* **16**, 515–519 (1990).
46. Mariscal-Becerra, L. *et al.* Luminescent characteristics of layered yttrium oxide nano-phosphors doped with europium. *J. Appl. Phys.* **121**, 125111 (2017).
47. Hardwick, L. J., Holzapfel, M., Novák, P., Dupont, L. & Baudrin, E. Electrochemical lithium insertion into anatase-type TiO₂: An in situ Raman microscopy investigation. *Electrochim. Acta* **52**, 5357–5367 (2007).
48. Cheng, X. L., Hu, M., Huang, R. & Jiang, J. S. HF-free synthesis of anatase TiO₂ nanosheets with largely exposed and clean 001 facets and their enhanced rate performance as anodes of lithium-ion battery. *ACS Appl. Mater. Interfaces.* **6**, 19176–19183 (2014).
49. Cao, Y., Li, Q., Li, C., Li, J. & Yang, J. Surface heterojunction between (001) and (101) facets of ultrafine anatase TiO₂ nanocrystals for highly efficient photoreduction CO₂ to CH₄. *Appl. Catal. B* **198**, 378–388 (2016).

50. Niu, X., Li, S., Chu, H. & Zhou, J. Preparation, characterization of Y³⁺-doped TiO₂ nanoparticles and their photocatalytic activities for methyl orange degradation. *J. Rare Earths*. **29**, 225–229 (2011).
51. Muktaridha, O., Adlim, M., Suhendrayatna, S. & Ismail, I. Progress of 3d metal-doped zinc oxide nanoparticles and the photocatalytic properties. *Arab. J. Chem.* **14**, 103175 (2021).
52. Dhanalakshmi, J., Iyyapushpam, S., Nishanthi, S. T., Malligavathy, M. & Padiyan, D. P. Investigation of oxygen vacancies in Ce coupled TiO₂ nanocomposites by Raman and PL spectra. *Adv. Nat. Sci. Nanosci. Nanotechnol.* **8**, 015015 (2017).
53. Ola, O. & Maroto-Valer, M. M. Review of material design and reactor engineering on TiO₂ photocatalysis for CO₂ reduction. *Photochem. Photobiol. C: Photochem. Rev.* **24**, 16–42 (2015).
54. Radha, E., Komaraiah, D., Sayanna, R. & Sivakumar, J. Photoluminescence and photocatalytic activity of rare earth ions doped anatase TiO₂ thin films. *J. Lumin.* **244**, 118727 (2022).
55. Lee, T. Y., Lee, C. Y. & Chiu, H. T. Enhanced photocatalysis from truncated octahedral bipyramids of anatase TiO₂ with exposed 001//{101} facets. *ACS Omega* **3**, 10225–10232 (2018).
56. Jiang, X. *et al.* Preparation of hollow yttrium-doped TiO₂ microspheres with enhanced visible-light photocatalytic activity. *Mater. Res. Express* **6**, 065510 (2019).
57. Wang, Y., Lu, K. & Feng, C. Photocatalytic degradation of methyl orange by polyoxometalates supported on yttrium-doped TiO₂. *J. Rare Earths*. **29**, 866–871 (2011).
58. Tao, X., Zhu, L., Wang, X., Chen, X. & Liu, X. Preparation of Zr/Y co-doped TiO₂ photocatalyst and degradation performance of hydroquinone. *Environ. Sci. Pollut. Res.* **29**, 40854–40864 (2022).
59. Zahoor, U. *et al.* Yttrium doped bismuth vanadate titania heterojunction for efficient photoreduction of Cr from wastewater under visible light. *Int. J. Environ. Res.* **16**, 88 (2022).
60. Żółtowska, S. *et al.* Thermal decomposition behaviour and numerical fitting for the pyrolysis kinetics of 3D spongin-based scaffolds. The classic approach. *Polym. Test.* **97**, 107148 (2021).
61. Valencia, S., Cataño, F., Rios, L., Restrepo, G. & Marín, J. A new kinetic model for heterogeneous photocatalysis with titanium dioxide: Case of non-specific adsorption considering back reaction. *Appl. Catal. B* **104**, 300–304 (2011).
62. Li, Y., Sun, S., Ma, M., Ouyang, Y. & Yan, W. Kinetic study and model of the photocatalytic degradation of rhodamine B (RhB) by a TiO₂-coated activated carbon catalyst: Effects of initial RhB content, light intensity and TiO₂ content in the catalyst. *Chem. Eng. J.* **142**, 147–155 (2008).
63. Kane, A. *et al.* g-C₃N₄/TiO₂ S-scheme heterojunction photocatalyst with enhanced photocatalytic Carbamazepine degradation and mineralization. *J. Photochem. Photobiol. Chem.* **430**, 113971 (2022).
64. Dudziak, S., Bielan, Z., Kubica, P. & Zielinska-Jurek, A. Optimization of carbamazepine photodegradation on defective TiO₂-based magnetic photocatalyst. *J. Environ. Chem. Eng.* **9**, 105782 (2021).
65. Achilleos, A., Hapeshi, E., Xekoukoulotakis, N. P., Mantzavinou, D. & Fatta-Kassinos, D. UV-A and solar photodegradation of ibuprofen and carbamazepine catalyzed by TiO₂. *Sep. Sci. Technol.* **45**, 1564–1570 (2010).
66. Chen, G. *et al.* Carbamazepine degradation by visible-light-driven photocatalyst Ag₃PO₄/GO: Mechanism and pathway. *Environ. Sci. Ecotechnol.* **9**, 100143 (2022).
67. Carabin, A., Drogui, P. & Robert, D. Photo-degradation of carbamazepine using TiO₂ suspended photocatalysts. *J. Taiwan Inst. Chem. Eng.* **54**, 109–117 (2015).
68. Nawaz, M., Miran, W., Jang, J. & Lee, D. S. One-step hydrothermal synthesis of porous 3D reduced graphene oxide/TiO₂ aerogel for carbamazepine photodegradation in aqueous solution. *Appl. Catal. B* **203**, 85–95 (2017).
69. Shahzad, A. *et al.* Heterostructural TiO₂/Ti₃C₂T_x (MXene) for photocatalytic degradation of antiepileptic drug carbamazepine. *Chem. Eng. J.* **349**, 748–755 (2018).
70. Kubiak, A. *et al.* The development of novel tailor-made photocatalytic reactor for sulfamethoxazole removal: Understanding mechanism and degradation pathway. *Chem. Eng. J.* **473**, 145168 (2023).
71. Kubiak, A. *et al.* A novel rapid microwave crystallization of photocatalysts for practical utility in the removal of phenol derivatives. *Ceram. Int.* **49**, 9104–9114 (2023).
72. Khan, I. *et al.* Efficient visible-light activities of TiO₂ decorated and Cr³⁺ incorporated-porous SmFeO₃ for CO₂ conversion and 4-chlorophenol degradation. *Surf. Interfaces* **34**, 102358 (2022).
73. Wu, Y. *et al.* B and Y co-doped TiO₂ photocatalyst with enhanced photodegradation efficiency. *J. Alloys Compd.* **695**, 1462–1469 (2017).
74. Yuan, R., Zheng, J., Guan, R. & Zhao, Y. Surface characteristics and photocatalytic activity of TiO₂ loaded on activated carbon fibers. *Colloids Surf. A: Physicochem. Eng. Asp.* **254**, 131–136 (2005).
75. Grzegórska, A. *et al.* Enhanced photocatalytic activity of accordion-like layered Ti₃C₂ (MXene) coupled with Fe-modified decahedral anatase particles exposing 1 0 1 and 0 0 1 facets. *Chem. Eng. J.* **426**, 130801 (2021).
76. Khan, I. *et al.* Bio-capped and green synthesis of ZnO/g-C₃N₄ nanocomposites and its improved antibiotic and photocatalytic activities: An exceptional approach towards environmental remediation. *Chin. J. Chem. Eng.* **56**, 215–224 (2023).
77. Hu, Z. *et al.* Construction of carbon-doped supramolecule-based g-C₃N₄/TiO₂ composites for removal of diclofenac and carbamazepine: A comparative study of operating parameters, mechanisms, degradation pathways. *J. Hazard. Mater.* **380**, 120812 (2019).
78. Benavente, E. *et al.* Application of CdTe quantum dots sensitized titanate nanotubes in photocatalytic degradation of organic pollutants under visible light irradiation. *J. Environ. Chem. Eng.* **11**, 110025 (2023).
79. Lopus, A. D. *et al.* Laddered type-1 heterojunction: Harvesting full-solar-spectrum in scavenger free photocatalysis. *Solar Energy* **240**, 57–68 (2022).
80. Kusiak-Nejman, E. & Morawski, A. W. TiO₂/graphene-based nanocomposites for water treatment: A brief overview of charge carrier transfer, antimicrobial and photocatalytic performance. *Appl. Catal. B* **253**, 179–186 (2019).
81. Li, H. *et al.* Recent advances in the application of bismuth-based catalysts for degrading environmental emerging organic contaminants through photocatalysis: A review. *J. Environ. Chem. Eng.* **11**, 110371 (2023).
82. Li, S. *et al.* Insight into enhanced carbamazepine photodegradation over biochar-based magnetic photocatalyst Fe₃O₄/BiOBr/BC under visible LED light irradiation. *Chem. Eng. J.* **360**, 600–611 (2019).
83. Franz, S. *et al.* Degradation of carbamazepine by photo(Electro)catalysis on nanostructured TiO₂ meshes: Transformation products and reaction pathways. *Catalysts* **10**, 169 (2020).
84. Nghia, T. H. *et al.* Removal of carbamazepine in aqueous solution by TiO₂ ceramic photo-catalyst under simulated solar light: Kinetics, effects of environmental factors and degradation pathways. *Water* **15**, 1583 (2023).

Acknowledgements

This work was funded by the National Science Centre of Poland (2023/07/X/ST5/00022).

Author contributions

A.K.: Conceptualization, Methodology, Formal analysis, Investigation, Data curation, Resource, Visualization, Funding acquisition, Project administration, Writing—Original Draft, Writing—Review & Editing; M.C.: Funding acquisition, Writing—Review & Editing, Supervision.

Competing interests

The authors declare no competing interests.

Additional information

Supplementary Information The online version contains supplementary material available at <https://doi.org/10.1038/s41598-023-51078-0>.

Correspondence and requests for materials should be addressed to A.K.

Reprints and permissions information is available at www.nature.com/reprints.

Publisher's note Springer Nature remains neutral with regard to jurisdictional claims in published maps and institutional affiliations.



Open Access This article is licensed under a Creative Commons Attribution 4.0 International License, which permits use, sharing, adaptation, distribution and reproduction in any medium or format, as long as you give appropriate credit to the original author(s) and the source, provide a link to the Creative Commons licence, and indicate if changes were made. The images or other third party material in this article are included in the article's Creative Commons licence, unless indicated otherwise in a credit line to the material. If material is not included in the article's Creative Commons licence and your intended use is not permitted by statutory regulation or exceeds the permitted use, you will need to obtain permission directly from the copyright holder. To view a copy of this licence, visit <http://creativecommons.org/licenses/by/4.0/>.

© The Author(s) 2024